J. Fluid Mech. (1998), *vol.* 369, *pp.* 273–299. Printed in the United Kingdom

Period tripling and energy dissipation of breaking standing waves

By LEI JIANG[1]†, MARC PERLIN[2] AND WILLIAM W. SCHULTZ[1]

[1]Department of Mechanical Engineering and Applied Mechanics, University of Michigan, Ann Arbor, MI 48109, USA

[2]Department of Naval Architecture and Marine Engineering, University of Michigan, Ann Arbor, MI 48109, USA

(Received 20 March 1997 and in revised form 18 March 1998)

We examine the dynamics of two-dimensional steep and breaking standing waves generated by Faraday-wave resonance. Jiang *et al.* (1996) found a steep wave with a double-peaked crest in experiments and a sharp-crested steep wave in computations. Both waveforms are strongly asymmetric in time and feature large superharmonics. We show experimentally that increasing the forcing amplitude further leads to breaking waves in three recurrent modes (period tripling): sharp crest with breaking, dimpled or flat crest with breaking, and round crest without breaking. Interesting steep waveforms and period-tripled breaking are related directly to the nonlinear interaction between the fundamental mode and the second temporal harmonic. Unfortunately, these higher-amplitude phenomena cannot be numerically modelled since the computations fail for breaking or nearly breaking waves. Based on the periodicity of Faraday waves, we directly estimate the dissipation due to wave breaking by integrating the support force as a function of the container displacement. We find that the breaking events (spray, air entrainment, and plunging) approximately double the wave dissipation.

1. Introduction

Synthetic Aperture Radar (SAR) images are often brighter near ocean features such as currents, shelves, and slicks that cause wave reflection and hence partial standing-wave systems. Since the backscattering of microwaves by the sea surface is sensitive to the curvature of surface features as well as Bragg periodicity, these strong SAR returns may be caused by higher surface curvature known to occur in standing waves that can be more peaked than progressive waves. Therefore, accurate representation of steep standing waves (or counter-propagating waves in general) is essential to the interpretation of SAR images. An even more complex phenomenon, wave breaking, directly influences the specular and Bragg scattering of electromagnetic radiation. Since counter-propagating waves are common in both open sea and coastal regions, their breaking mechanisms are crucial to wave modelling, both deep water and shoaling wave-breaking criteria, and energy dissipation. To this end, the breaking standing wave and its energy dissipation serve as a good model to study.

A standing gravity wave on the free surface of an irrotational, inviscid deep liquid

† Present address: Intel Corp. M/S RA1-305, 5200 NE Elam Young Parkway, Hillsboro, OR 97124, USA.

has been described analytically by Penney & Price (1952) and Schwartz & Whitney (1981). Based on the Stokes expansion, their solutions describe a standing wave with a shape ranging from sinusoidal at modest amplitudes to one with a more peaked crest and a flatter trough at higher amplitudes. The experiments of Taylor (1953) seem to verify Penney & Price's conjecture of a 90° crest angle for the extreme waveform. However, studies by Schultz & Vanden-Broeck (1990) and Mercer & Roberts (1992) suggested that the steepest wave has a crest sharper than 90°. Schultz & Vanden-Broeck (1990) and Schultz *et al.* (1998) further showed that standing waves with very small surface tension can exhibit wave steepness much higher than the limiting wave steepness of gravity waves. Steep gravity–capillary standing waves feature a flat crest and sometimes a bulbous protuberance.

In his experiments, Taylor (1953) generated standing waves by simultaneously oscillating two hinged vertical paddles. Standing waves can also be excited by vertical oscillation through subharmonic resonance, i.e. Faraday waves (Benjamin & Ursell 1954; Miles & Henderson 1990). The linear stability of Faraday waves is described by the detuning parameter p and forcing parameter q

$$p = \frac{4\omega_i^2}{\omega_f^2},\ q = 2Fk_i \tanh k_i h,$$

where ω_f is the forcing frequency and F is the forcing amplitude. The linear natural frequency is defined by $\omega_i = \left[gk_i(1+\kappa k_i^2)\tanh(k_i h)\right]^{1/2}$, where h is the water depth, k_i is the wavenumber and $\kappa = \sigma k^2/\rho g$ is the dimensionless inverse Bond number. Here σ represents surface tension, ρ represents fluid density, and g is the gravitational acceleration. The subharmonic resonance corresponds to $p \approx 1$ for the ith spatial mode with wavenumber $k_i = 2\pi i^2 \lambda^{-1}$, where λ is the fundamental wavelength. In the following, we denote the linear natural (cyclic) frequency for the fundamental mode by $f_N = \omega_1/2\pi$.

Owing to the laterally fixed vertical endwalls, Faraday-wave experiments more accurately model the spatial periodicity of standing waves. Schultz *et al.* (1998) adopted this approach and found good agreement with their calculation when the amplitude dispersion curve for free standing waves, $\omega = \omega(H/\lambda)$, is closely followed in the experiments. The nonlinear wave (radian) frequency ω is a function of wave steepness H/λ, where H is the wave height and λ is the wavelength. Three-dimensional effects that prevented Taylor from obtaining steeper waves are avoided by using a rectangular tank with a large aspect ratio.

Steep waves can be generated with a frequency close to the linear natural frequency f_N by simply increasing the amplitude of the vertical forcing. Jiang *et al.* (1996) found that dimpled crests appear in the steep wave profile and the waveforms become asymmetric in time. An example is shown later in figure 6. Temporal symmetry is broken by dissipation, but obvious asymmetries occur only for steep waves with dimpled crests. Jiang *et al.* (1996) further demonstrated through both experiments and fully nonlinear simulation that the interaction between the first two temporal harmonics is responsible for the appearance of dimpled crests and strong temporal asymmetry. These steep waveforms disagree with Taylor's experiments and are not described by any nonlinear standing wave models. Previous asymptotic analyses are valid only when resonance between different harmonics can be 'avoided' (Tadjbakhsh & Keller 1960). Likewise, symmetry in time is either implicitly or explicitly assumed in asymptotic expansions (Schwartz & Whitney 1981) and numerical solutions (Mercer & Roberts 1992). Recently Bryant & Stiassnie (1994) discussed multiple

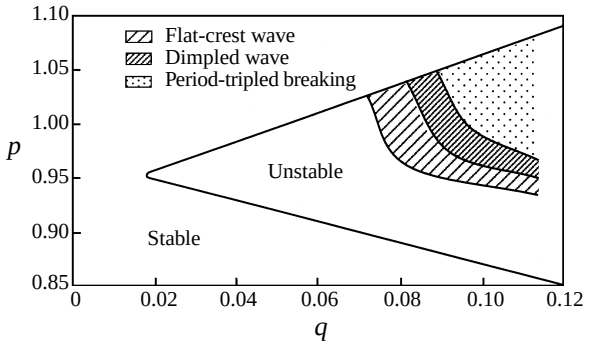

FIGURE 1. Locations in parameter space of the various waveforms in Faraday-wave experiments. The solid line represents the neutral-stability curve measured from experiments.

solutions of small-amplitude standing waves due to harmonic resonance using the Zakharov equations. We thus expect harmonic interaction to be more significant when standing waves become strongly nonlinear, leading to new waveforms.

Steep standing waves undergo a surprising transformation at even larger forcing. Small plunging breakers first appear to each side of the dimpled crest. A further increase in forcing amplitude leads eventually to period tripling with breaking every two out of three waves. The existence regime for period tripling is shown in figure 1 – an improvement of the p, q diagram of Jiang *et al.* (1996). The stability boundary should be centred around $p = 1$; however, the measured neutral-stability curve in figure 1 is shifted downward due to contact-line effects (Jiang *et al.* 1996). Here, all experiments including those with period-tripled breaking are limited to within the neutral-stability curve.†

This paper is organized as follows. The experimental techniques are described in § 2. To estimate the wave dissipation, especially dissipation due to breaking, we measure directly the energy–dissipation balance (§ 2.2). Temporal asymmetry and strong second temporal harmonics are first shown in § 3 for steep waves without breaking. The three distinct wave forms during period-tripled breaking are then described in § 4 and compared with non-breaking waves. From Fourier analysis and complex demodulation, we gain additional insight into the dynamics of period tripling, particularly the interaction between the fundamental mode and its second temporal harmonic (§ 4.3). Results of direct dissipation measurements are presented for both non-breaking and breaking waves in § 5.

2. Experimental techniques and apparatus

We use essentially the same experimental setup as Jiang *et al.* (1996) with the addition of a load cell described in § 2.2. Figure 2 shows all relevant hardware except for the shafts and linear bearings positioned outside the tank for lateral support. The tank is guided vertically by six rolling stabilizers (two on the front, two on the sides and two on the rear) to reduce lateral displacement. The inner dimensions of

† Due to hysteresis effects, waves can be generated even with $p > 1$ and (p, q) lying outside the neutral-stability curve by continuously changing forcing frequency or forcing amplitude. The hysteresis can be caused by either contact-line effects as shown by Jiang *et al.* (1996) or by the intrinsic nonlinear effect of standing waves (Decent & Craik 1995). The present experiments all start from quiescent condition with fixed forcing amplitude and frequency. Therefore no data are obtained when (p, q) lie outside the neutral-stability curve.

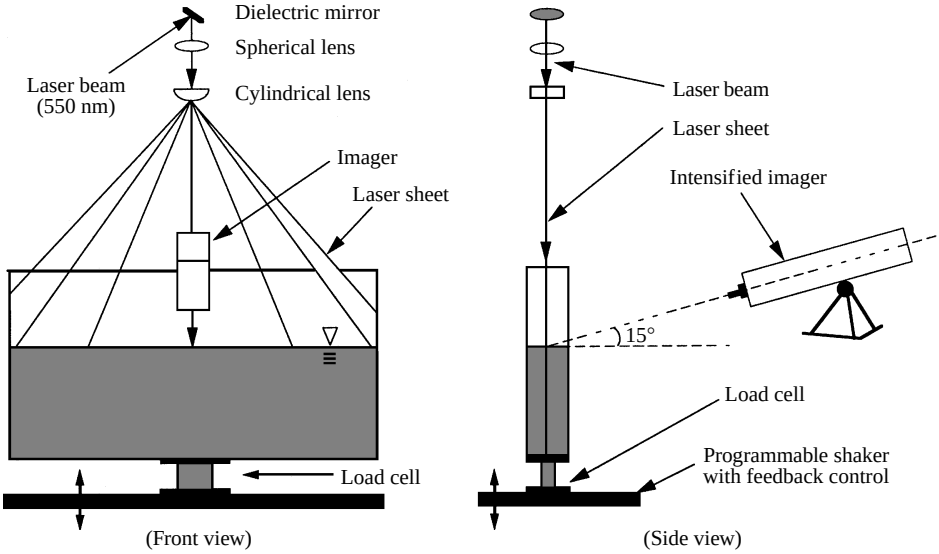

FIGURE 2. Experimental schematic of the tank, illumination, and imaging system (not to scale). The spherical lens has a focal length of 1000 mm, the cylindrical lens has a focal length of 6.35 mm.

the rectangular glass tank are 600 mm long, 60 mm wide and 483 mm deep. The water depth is approximately 300 mm. With negligible lateral vibration (less than 3% of the vertical excitation), this 10:1 tank aspect ratio ensures that the waves are two-dimensional. We generate the fundamental wave mode ($k = k_1$) with one wavelength in the tank to preserve spatial symmetry about the tank centreline.

The natural frequency of the 60 cm wave is $f_N = \omega_1/2\pi = 1.611$ Hz. The forcing frequencies are within the range $2f = 3.24 \pm 0.10$ Hz where f represents the frequency of the forced subharmonic wave. The tank is fixed to a programmable shaker that is best suited to operate in a low frequency range: 0.5 Hz to 5.0 Hz. The shaker is driven by a brushless servo motor with a low-mass, high-performance Magnequench armature. The driving mechanism is a ball-screw assembly. A linear response is obtained for forcing amplitudes between 1 mm and 10 mm. The control system includes a Macintosh computer with National Instruments' LabVIEW software, data acquisition boards, and a transducer that measures the vertical displacements of the tank. More details about the shaker setup can be found in Jiang *et al.* (1996). In a typical feedback signal, shaker displacement amplitudes of the second, third, and fourth harmonics are 0.6, 2.8 and 0.3% of the fundamental harmonic amplitude. The relatively large third-harmonic forcing was also reported in Jiang *et al.* (1996), but its magnitude is not altered by the presence of wave excitation and is therefore a natural characteristic of the wavemaker. The corresponding third-harmonic wave response is negligible as shown in Jiang *et al.* (1996) and in the wave spectrum of § 4.2.

2.1. *Wave measurements*

Spatial surface profiles are obtained by a laser-sheet measurement technique (Perlin, Lin & Ting 1993). The imaging system in figure 2 includes a 5 W Argon-Ion laser, attendant optics and a high-speed, 8-bit video system with an intensified imager. We use a spherical lens to focus the laser beam and a cylindrical lens to expand the laser beam into a sheet. The laser sheet is introduced from above the water, parallel to the front glass wall. It illuminates the central plane of the tank with a thickness less than

0.5 mm at the still water level. The added dye (fluorescein) in the water fluoresces under the laser sheet and generates a light-intensity jump at the free surface. In experiments with complicated breaking wave forms, we also use silver-coated hollow glass spheres (10 μm mean diameter) as seeding particles to better illuminate the entire central plane below the free surface.

To help avoid surface contamination, the tank is scrubbed before and after each use with ethyl alcohol. Our treated water is de-ionized, carbon-adsorbed, and 0.2 micron filtered to maintain a surface tension of 72 dynes cm^{-1} at room temperature, close to that for pure water. The surface tension decreases to about 71 dynes cm^{-1} after the addition of fluorescein. By comparing video images of steep standing waves with and without dye, we verify that the small change in surface tension does not cause perceptible changes in the wave profiles. The surface tension is further reduced by less than 0.5 dynes cm^{-1} with particles in the water (Ting & Perlin 1995). The particles are only used to illustrate features of breaking waves. Addition of dye also increases the wave damping from 0.05 s^{-1} to 0.07 s^{-1} as shown in Jiang *et al.* (1996). However, the qualitative behaviour of standing wave breaking does not appear to be affected by either particle or dye addition.

We use a Kodak Ektapro CID intensified imager with controller to record the wave profile and use the Ektapro EM 1012 recorder for storage. The image is composed of 239 horizontal pixels by 192 vertical pixels. To capture the entire surface, we use a 50 mm camera lens on the intensified imager with the camera located approximately 2.6 m from the tank. Its optical axis is oriented perpendicular to the intersection of the laser sheet and the quiescent water surface and at about a 15° angle with respect to the mean water surface (to remove any obstructing influence from the meniscus on the front glass wall). Using a precise target shows no significant image distortion of the surface in either direction. The average image resolution for this experimental setup is 2.66 mm/pixel and the measurement error is about one pixel. The recording speed is chosen from 50 frames/s to 250 frames/s. The images are transferred to computer via a standard GPIB interface and the wave profiles are then extracted from the images using an edge-detection program and running-average smoothing.

For the time histories of surface elevation at the tank centre, we use a fixed capacitance-type wave probe with an outside diameter of 1.6 mm positioned at the horizontal centre of the tank. The measurement error is less than 1% of the typical wave height. The probe and feedback signals are low-pass filtered using two Krohn–Hite model 3342 analog filters with a cutoff frequency of 30 Hz. Then, the feedback signal is subtracted from the probe signal to obtain the actual surface elevation with respect to the tank.

2.2. *Force and wave dissipation determination*

The support force is measured by an Omega LCCA-100 load cell (strain gauge) placed beneath the tank centroid and on the shaker (see figure 2). Its specifications in percentage of full scale are: 0.03% nonlinearity, 0.02% hysteresis, and 0.02% non-repeatability. The load cell has a maximum capacity of 445 N, sufficient for the total weight of tank and water (294 N) and the accelerations used. To obtain accurate work estimates, both the force and displacement signals are sampled at 300 Hz. The two time series are processed by the same dual-channel Krohn–Hite 3342 low-pass filter with the same cut-off frequency (100 Hz) to avoid phase lag. (The measured force contains higher harmonics in the range of 12 Hz to 25 Hz that are attributed to the natural vibration of the tank and shaker.) We obtain the energy (work) input to the system by integrating force with respect to the tank displacement using the

Stage	Wave field	Work–dissipation balance
1	None excited	W_1 = mechanical loss
2	Wave growth	$W_2 = W_1 + \Delta E(t) + \mathscr{D}(t)$
3	Periodic waves ($F < F_b$) or double-plunger periodic breaking ($F \approx F_b$) or quasi-periodic breaking ($F > F_b$)	$W_3 = W_1 + \mathscr{D}(t)$

TABLE 1. Three stages of wave excitation and the corresponding W_i, work per unit wave period. $\Delta E(t)$ and $\mathscr{D}(t)$ represent energy increase and wave dissipation over one wave period, respectively. F_b is the threshold shaker stroke amplitude for breaking.

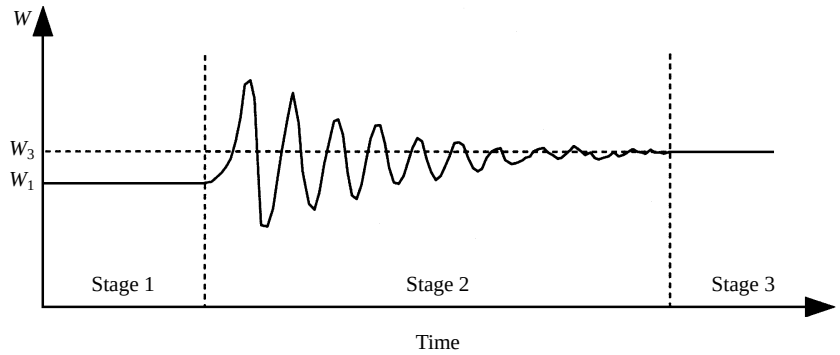

FIGURE 3. Schematic of the work input as a function of time during a complete experiment with fixed forcing parameters.

trapezoidal rule. Dissipation due to wave motion and breaking is then estimated using the following procedure.

A complete experiment at fixed forcing parameters unfolds in three stages (table 1 and figure 3). The measured work per unit wave period (W_i for each stage $i = 1, 2, 3$) is separated into wave energy (E), wave dissipation ($\mathscr{D}$) and mechanical losses. In stage 1, the tank is oscillated but no wave growth is observed; therefore both the wave energy E and the wave dissipation $\mathscr{D}$ are negligible. W_1 represents the mechanical losses due to bearing dissipation, friction and other forces that are unrelated to the fluid motion in the tank. During wave growth (stage 2), W_2 typically overshoots and then slowly decays to a new finite value (figure 3). Part of this work input is converted into wave energy $E(t)$. Determining the wave energy $E(t)$ is generally difficult; however, an estimate of $\mathscr{D}$ can be obtained from stage 3 that does not require the value of $E(t)$. Since the wave field is periodic in stage 3, E remains constant and W_3 is balanced by wave dissipation $\mathscr{D}$ and mechanical loss. Assuming that the mechanical loss is equal to that in the first stage, W_1, the wave dissipation is then determined by $\mathscr{D} = W_3 - W_1$.

Typical force–displacement diagrams are shown in figures 4(a) and 4(b) representing W_1 and W_3, respectively. Two work cycles (two forcing periods) are shown in each diagram, and each cycle can be divided into four areas representing positive and negative work. The four areas reflect the existence of higher force harmonics due to mechanical vibrations. Comparison of figures 4(a) and 4(b) shows the dominance of mechanical losses (W_1) in the total work and a larger work input in stage 3 because of the wave dissipation. The force–displacement curves in figure 4(b) are slightly different

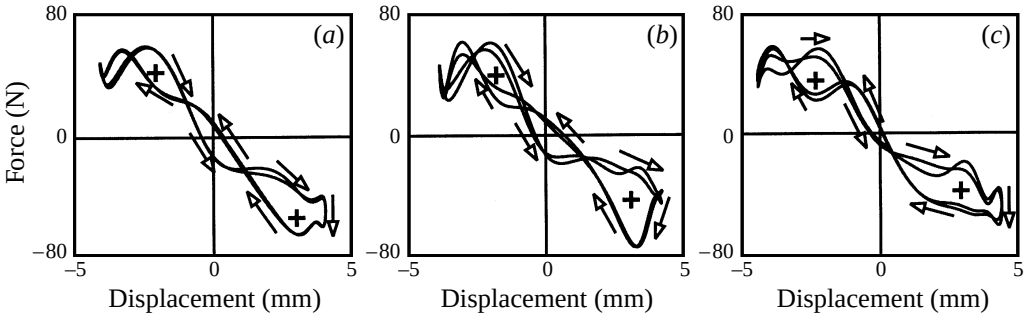

FIGURE 4. The force–displacement diagrams during two consecutive forcing cycles (one wave cycle). +, Positive work area. Areas without sign represent negative work. The arrows denote loop direction. $f = \omega/2\pi = 1.60$ Hz. (*a*) Stage 1 ($F = 4.15$ mm), no wave excited, (*b*) Stage 3 ($F = 4.15$ mm), periodic wave field without breaking. (*c*) Stage 3 ($F = 4.51$ mm), period-tripled breaking. Note that F in (*c*) is different from F in (*a*, *b*).

during two consecutive forcing cycles.† However, the total work (net positive area) for each forcing cycle differs only by 1%. A low-pass filter with a cut-off frequency of 30 Hz is applied for smoothing.

The aforementioned technique is based on a balance between energy input and energy dissipation, and therefore it only applies to periodic wave fields. Breaking-wave dissipation would be difficult to measure because of the irreversible breaking process. Fortunately, the breaking waves in our experiments are periodic! Near the threshold forcing amplitude F_b, Jiang *et al.* (1996) observed double plungers at the crest, but the waveform remains temporally and spatially periodic. Period-tripled breaking appears at a slightly larger forcing with breaking waves every two out of three wave cycles as will be shown in § 4. The energy balance for breaking waves is then similar to that for non-breaking waves (table 1), except that $\mathscr{D}$ represents the breaking-wave dissipation averaged over three wave periods. Figure 4(*c*) shows W_3 during period-tripled breaking and a corresponding increase in the work input owing to breaking-wave dissipation. The work loop over one wave cycle is shown here. The force–displacement curves for all three breaking-wave modes shown in § 4 are qualitatively similar to figure 4(*c*) with slightly different net positive areas.

Owing to bearing friction and other friction caused by the start-up process, the integrated work per wave cycle (W_1) has a 7% standard deviation. For non-breaking periodic waves, the standard deviation of W_3 is 2.5%. For the triply-periodic breaking, however, the standard deviation increases due to the unsteady nature of breaking. Dissipation rates are discussed in § 5.

3. Steep standing waves

We first discuss the steep Faraday wave, as its waveform and temporal asymmetry are related directly to wave breaking discussed later. The spatial and temporal

† The measured forces at t_0 and $t_0 + T/2$ (where T is the temporal wave period) are not quite the same even though the tank motion nominally repeats after one half wave period. For non-breaking, periodic waves, we observed approximately the same profile at t_0 and $t_0 + T/2$ with a $\lambda/2$ horizontal shift (see figures 15, 16, and 17 in Jiang *et al.* 1996). Integrated wave properties should then be $T/2$-periodic, including the wave-induced pressure on the tank bottom and the friction on the front and back walls. The different force measurement in the two half wave periods (figure 4*b*) is probably caused by the boundary layers on the two endwalls where this temporal half-periodicity is broken.

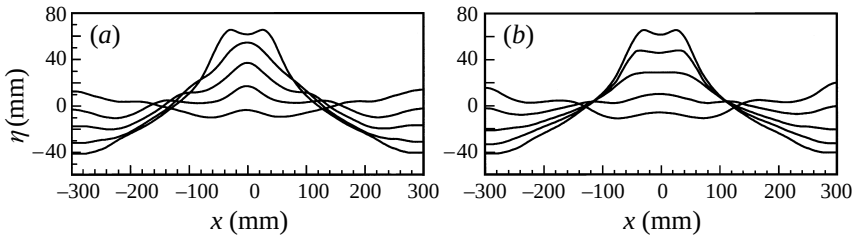

FIGURE 5. Experimental wave profiles with (*a*) increasing and (*b*) decreasing elevation at the centreline. The time interval between each profile is 0.04 s. $f = \omega/2\pi = 1.615$ Hz, $F = 3.85$ mm. (From Jiang *et al.* 1996.)

symmetries are defined by $\eta(x,t) = \eta(x,-t) = \eta(-x,t)$ where a crest occurs at $x = 0$, $t = 0$. Both symmetries are preserved in the Penney & Price (1952) solution. Jiang *et al.* (1996) observed Faraday waves that are significantly asymmetric about $t = 0$. Typical profiles extracted from figure 17 of Jiang *et al.* (1996) are shown in figure 5. The wave crest is more peaked (figure 5*a*) for increasing elevation at $x = 0$, but a dimpled crest appears and remains for decreasing elevation at $x = 0$ (figure 5*b*). These waves appear when the wave steepness H/λ exceeds 0.15. Here H represents the peak-to-peak wave height measured at $x = 0$.

The dimpled crest and broken temporal symmetry reflect the interaction between the fundamental mode and its second harmonic in time. To illustrate this, we express the surface elevation $\eta(0, t)$ for periodic waves with frequency ω as

$$\eta(x = 0,\, t) = \eta_0 + a_1 \cos(\omega t + \theta_1) + a_2 \cos(2\omega t + \theta_2) + \cdots, \tag{3.1}$$

where the phase shifts of the first and second harmonic are θ_1 and θ_2 and the associated amplitudes are a_1 and a_2, respectively. The time-averaged elevation η_0 is non-zero for finite-amplitude waves. The phase-shift difference $\theta_2 - 2\theta_1$ is defined to be within $[0, 2\pi)$. Penney & Price (1952) restricted the second harmonic to be higher order and $\theta_2 - 2\theta_1 = 0$. Therefore their solution describes a non-dimpled crest even for steep waves. The temporal symmetry is preserved in (3.1) only for $\theta_2 - 2\theta_1 = 0$ or π.

Harmonic amplitudes and phases shown in figure 6 are obtained from Fourier analysis of the measured $\eta(0, t)$. Although the phase angles θ_2 and θ_1 depend on the starting point of a particular time series, the phase-shift difference $\theta_2 - 2\theta_1$ does not and remains constant in time for periodic waves. Figure 6(*c*) shows this phase shift as a function of the forcing amplitude. The forcing frequency is fixed at 3.22 Hz. After the wave crest becomes flat, $\theta_2 - 2\theta_1$ decreases steadily with increasing forcing amplitude. Values other than zero or π indicate temporal asymmetry even at moderate wave amplitudes (small forcing). These waves appear symmetric only because a_2 is insignificant as shown in figure 6(*b*). Increasing nonlinearity leads to larger a_2 and a dimpled crest. The temporal asymmetry then becomes apparent for larger forcing. The amplitude ratio a_2/a_1 in figure 6(*b*) grows more slowly for increasing F when breaking occurs ($F > 4.60$ mm in figure 6*a*). Note that when period-tripled breaking occurs, additional terms corresponding to the $f/3$ frequency should be added to (3.1). The harmonic amplitudes and phases shown in figure 6 only represent averaged values over the FFT window.

The numerical simulation of Jiang *et al.* (1996) reveals a different steep waveform with a sharply peaked crest at the maximum position (see their figure 19). The sharp crest reflects a different pattern of temporal-symmetry breaking, i.e. the phase-shift

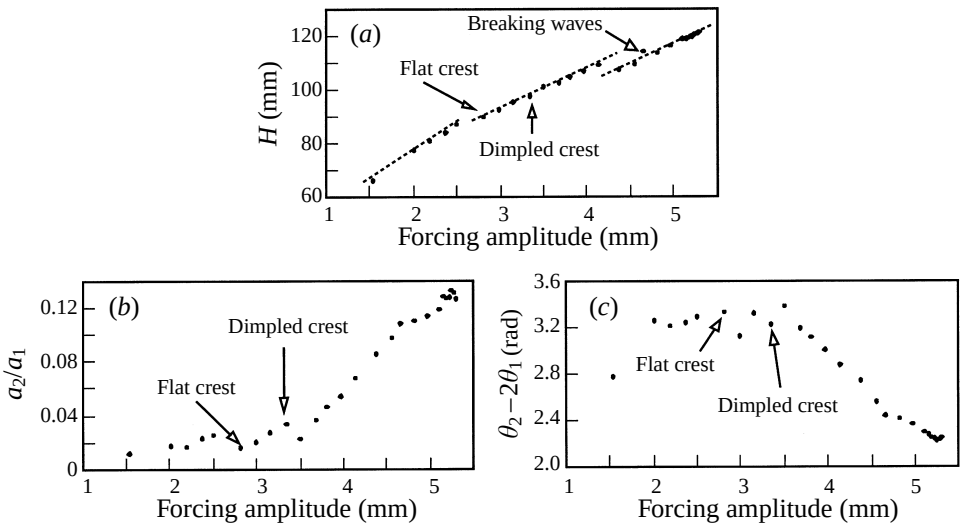

FIGURE 6. Effect of forcing amplitude on waveforms ($f = \omega/2\pi = 1.61$ Hz). (*a*) Wave height H, (*b*) ratio of the harmonic amplitudes a_2 and a_1, (*c*) phase-shift difference $\theta_2 - 2\theta_1$.

difference $\theta_2 - 2\theta_1$ is neither zero nor π nor the value obtained above for the dimpled wave form. These differences may be due to the inadequate Rayleigh-damping model used by Jiang *et al.* (1996). However, the interaction between harmonics is apparent in both experiments and numerics, and the disparate forms of steep standing waves may indicate multiple solutions. The importance of harmonic interaction will be examined again using complex demodulation in the discussion of standing wave breaking (§ 4.3).

4. Breaking standing waves

There are essential differences between breaking in unidirectional travelling waves and standing waves. Travelling gravity waves seldom attain the limiting Stokes waveform prior to the initiation of breaking. One mechanism for the breaking of a single travelling wave is the superharmonic instability that leads to front-face steepening and the formation of a spilling breaker or a plunging breaker. Crest asymmetry also exists for short gravity and gravity–capillary wavelengths with parasitic ripples on the front face (e.g. Longuet-Higgins 1963; Perlin *et al.* 1993).

Asymmetric breaking is less likely to occur in a standing wave because of its inherent spatial symmetry. When gentle breaking occurs for standing waves, a spiller forms at the crest before it changes into a dimpled form and a subsequent double plunger breaks outward from the centre (figure 21 in Jiang *et al.* 1996). These waves are still periodic in time and the wave crest maintains its spatial symmetry. The wave profile remains two-dimensional except at the crest region where breaking occurs. (In Taylor 1953, the extreme standing waves were three-dimensional because of a moderate tank aspect ratio of 2.17:1.) Because of the dimpled crest, the limiting wave steepness has a somewhat ambiguous definition. A capacitance probe at $x = 0$ gives $H/\lambda \approx 0.193$ at incipient breaking (figure 6*a*), while the peak-to-trough height from the spatial profile is $H/\lambda \approx 0.21$ (Jiang *et al.* 1996). The latter value is very close to the limiting height for a free standing wave (Schwartz & Whitney 1981; Mercer & Roberts 1992) even though the waveforms are significantly different.

A dimpled wave crest with small-scale breaking remains seemingly periodic in time

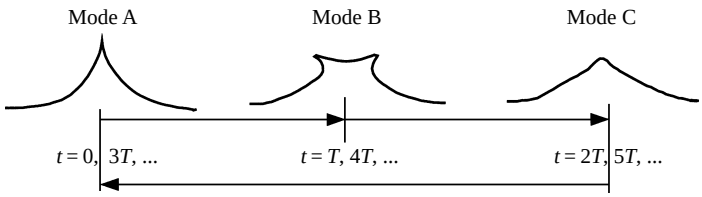

FIGURE 7. Illustration of three different modes during period-tripled breaking. T is the temporal wave period before period tripling (twice the forcing period). Each crest feature appears at the endwalls of the tank $1.5T$ after it appears at the centreline.

when the forcing amplitude is close to, but less than, a critical value F_b. Above this threshold, however, the gentle breaking gives way to period-tripled breaking: the subharmonic wave on an initially flat surface again develops a dimpled crest, but now never becomes truly periodic before the sharp crest appears and violent breaking follows. Our fully nonlinear Cauchy-integral method fails near wave breaking and therefore cannot predict the observed period tripling. We now focus on the experimental results.

4.1. *Period-tripled breaking: spray and splash*

The period-tripled breaking consists of three distinct modes: A, B, and C, as illustrated in figure 7. The maximum wave profile in mode A is characterized by its high elevation, sharp crest angle and violent breaking and drop formation. Mode B follows with a dimpled or flat crest and double plungers to the sides of the crest. Mode C has a round (non-breaking) crest similar to Penney & Price's (1952) solution. The sharp-crested mode A reappears after mode C, forming a recurrent cycle with a three-wave period. The mode-A wave was never realized in our experiments on steep, non-breaking waves.

A series of images recorded at 50 Hz shows the three breaking modes for a forcing amplitude of 4.60 mm and a forcing frequency of 3.20 Hz. Mode A (figure 8*a*) has a sharp crest angle *less* than 30°. The geometry of the maximum wave profile is similar to the hyperbolic waves predicted by Longuet-Higgins (1980). Water is ejected at the maximum crest elevation (figure 8*a*, $t = 0.20$ s) and forms columnar drops. The jet then eventually collides with the water surface, first forming a crater, then a rebounding jet and entrained air (bubbles). Significant acoustic energy is generated at this instant. Splashes, remnants of the impinging process, are obvious in the first frame of figure 8(*c*). (Note that we have not separated the sets of images by the exact underlying wave period $T = 0.62$ s, nor have we presented an entire three-wave-period sequence.) The rebounding jet at the tank centre lasts more than half a wave period, from 0.44 s to 0.76 s, creating turbulent motion at the wave crest. The stronger double plungers to each side of the crest (0.72 s) enhance dissipation in the entire wave field as compared to mode C (figure 8*e*, *f*), which has no energetic breaking. Note that the last image of figure 8(*f*) shows mode B at the endwalls $1.5T$ after it occurs at the tank centreline ($t = 0.72$ s).

Mode A is essentially two-dimensional. Except for small perturbations, modes B and C are uniform along the tank-width direction as well. A similar sequence of breaking occurs at the tank endwalls with a phase difference of $1.5T$. However, the maximum elevation is not as high as that at the tank centre ($t = 1.04$ s in figure 8*d*), jets are only formed occasionally, and the subsequent splash is less intense. All these can be attributed to the viscous boundary layer and the stabilizing effect of the wall.

In fact, avoiding sidewall boundary layers near the wave crest was our motivation for studying the fundamental (full-wavelength) mode rather than the sloshing (half-wavelength) mode.

Figure 9 shows the edge-detected profiles corresponding to figure 8. The limiting profile in mode A has a wave crest 140 mm above the mean water level (figure 9*a*). This elevation far exceeds the maximum elevation for incipient breaking ($\approx$ 86 mm as shown in Jiang *et al.* 1996). The remnants of breaking and air entrainment from previous wave cycles appear as ripples in figure 9(*a*) before the maximum elevation is reached. In mode B, the slightly asymmetric breaking plungers conceal the wave profile immediately below on each side of the flat crest. (This shortcoming is corrected in figure 12.) Figure 10 shows the spatial wavenumber spectrum for the entire series of profiles in figure 9 (38 in total). Both the maximum amplitude and the median amplitude over three wave periods are presented for each spatial harmonic. Only the first 30 harmonics are shown as the smoothing procedure in the edge detection makes it impossible to represent higher harmonics caused by the sharp crest (mode A) or the double plungers (mode B). Nonetheless, the broad spectrum and the slow amplitude decay with increasing wavenumber reflect the strong nonlinearity in the breaking waves. It is difficult to distinguish the dominant higher harmonics from figure 10. Only the first three harmonics have significant median amplitude over three wave periods, but the maximum amplitudes of the first 10–12 harmonics are larger than the forcing amplitude. Therefore our analysis on harmonic interaction will be focused on temporal harmonics (§ 4.3).

Remaining focused on the spatial details, we examine the sharp wave in figure 11 with an average resolution of 0.4 mm/pixel. At $f = 1.60$ Hz, small ripples appear on the slightly asymmetric crest (the last two frames in figure 11*a*) before the crest descends and disintegrates into a water jet. The break-up process is slightly different for $f = 1.61$ Hz (figure 11*b*). The crest is sharper, and a small water jet forms before the maximum crest elevation is reached. The subsequent water jet is significantly less than that for $f = 1.60$ Hz, creating spray. The jet collision in period-tripled breaking is generally more intense at lower wave frequencies, e.g. $f = 1.59$ Hz and $f = 1.60$ Hz. These differences in the breaking process are shown in § 5 to explain the frequency effect in the total wave dissipation.

Although the first sharp crest forms an upward jet in mode A, it can also develop into a large plunger with its crest listing to one side. The appearance of an upward jet or an asymmetric plunger is random and does not affect the triple periodicity. A 'leftward' plunging breaker (figure 12*a*) is captured with both seed particles and dye in the water so that both the free surface and the underlying water are illuminated (§ 2.1). The bright rays in figure 12 are caused by refraction of the laser sheet at large free surface curvature. Using the same technique, we demonstrate mode-B breaking in figure 12(*b*). Double plungers form at each side of the flat crest and create local 'bores' (0.02 and 0.04 s). These post-breaking plungers 'slide down' the wave crest at 0.06 and 0.08 s, creating irregular motions near the surface. The bulbous centre at 0.04 to 0.08 s is caused by the rebounding jet initiated in the previous part of the wave cycle. The bright spots beneath the wave crest (the last four frames) are entrained air bubbles. Mode C has the least breaking as shown in figure 8, and usually no irregular surface motions are observed as shown in figure 12(*c*).

4.2. *Phase portrait and spectral analysis*

To further illustrate the bifurcation from periodic waves to triply-periodic breaking, the pseudo-phase plane of the mid-tank elevation signal with a delay of $\tau = 0.10$ s

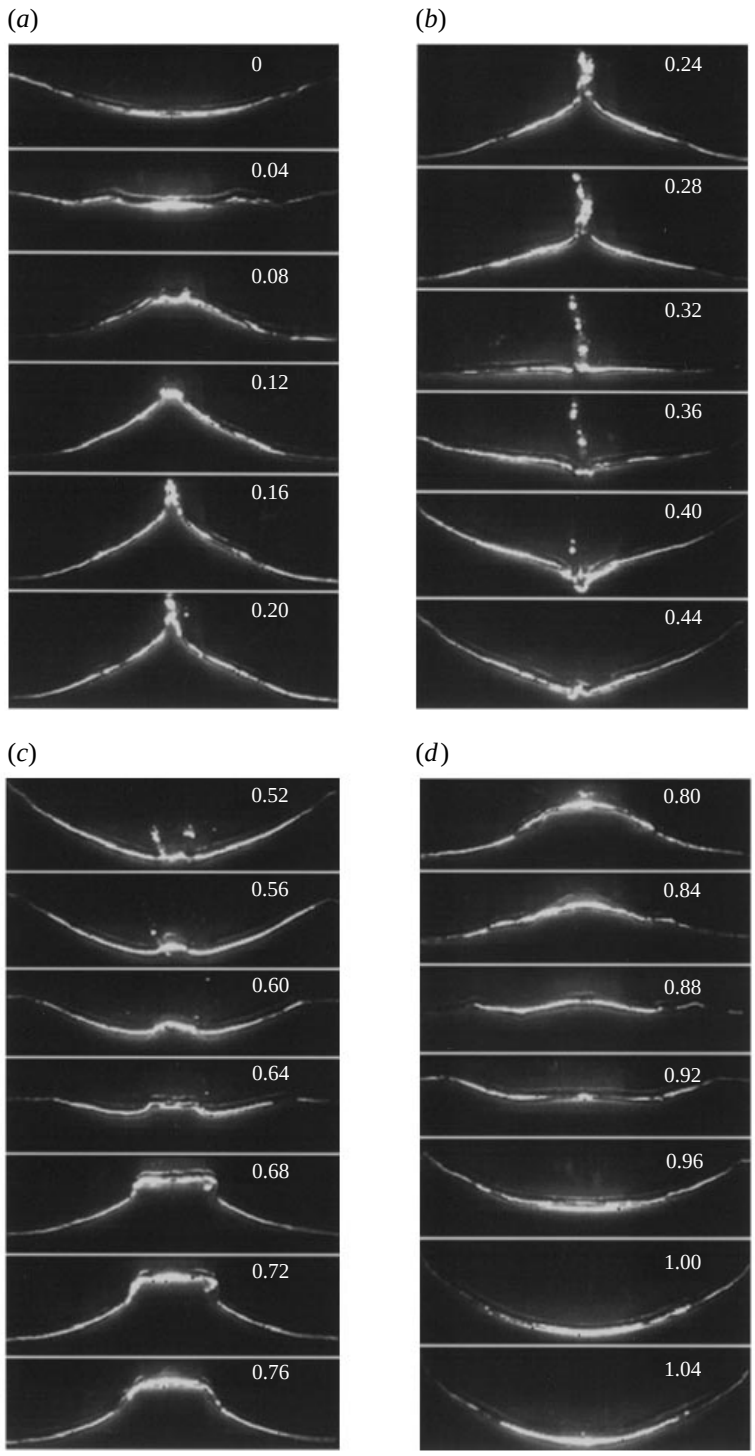

FIGURE 8(*a–d*). For caption see facing page.

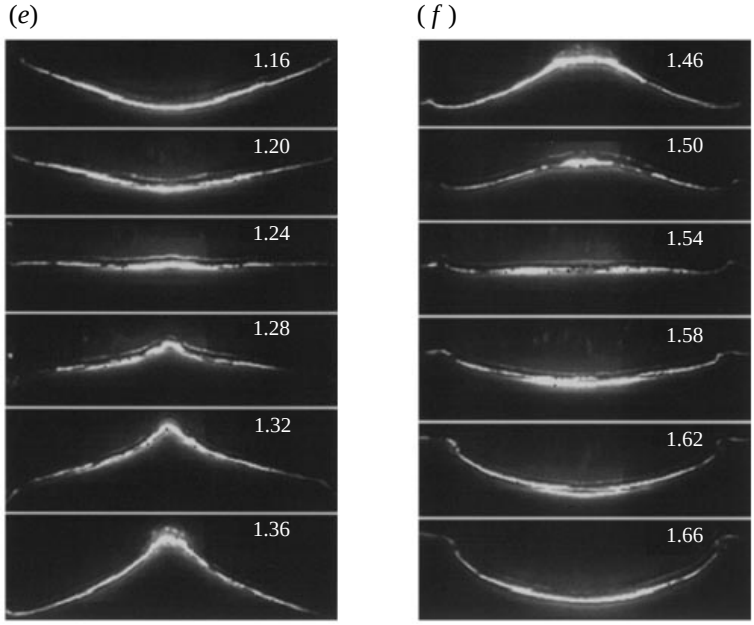

FIGURE 8. The observed waveform during (*a*) ascending and (*b*) descending phases of mode A; (*c*), (*d*) same for mode B; (*e*), (*f*) same for mode C. $F = 4.6$ mm, $f = 1.60$ Hz. The image width is 600 mm (the entire wavelength) with no vertical exaggeration. The numbers shown in the images represent time in s.

(30 data points for the 300 Hz sampling rate) is shown in figure 13. We apply a 30 Hz low-pass filter to the time series and use a record of 50 wave cycles (9375 data points) to construct the time-delay-coordinate portraits (embedding-space method, e.g. Moon 1992). The reconstructed pseudo-phase portrait is topologically equivalent to the phase plane with the elevation and its derivatives as coordinates (Packard *et al.* 1980; Takens 1980). Determining *a priori* the embedding dimension and the time delay τ is not trivial. For simplicity, we first restrict the reconstructed phase space to be two-dimensional, i.e. $\eta(t)$ versus $\eta(t+\tau)$, even though the observed period tripling may result from higher-dimensional dynamics. In principle, the topology of the pseudo-phase plane is equivalent for different delay intervals τ (Mullin 1993) if the embedding dimension is sufficiently large. A delay time of $\tau = 0.16T$ is chosen here such that variations in the orbits are not obscured by noise in the elevation signal.

The steep non-breaking wave ($F = 4.15$ mm) corresponds to a single orbit in phase space, with clearly identifiable superharmonics in the spectrum (figure 13*a*, *b*). The subharmonic component ($f = 1.60$ Hz) dominates, but there exists obvious second harmonic content. Amplitudes of the third and fourth harmonics are an order of magnitude lower that that of the second harmonic. 'Noise' in the phase orbit is partly attributed to the small modulations exhibited in figure 13(*b*) as low spectral peaks. As these spectral peaks are closely spaced at $f/3$ intervals, we might expect period-tripling modulation before breaking. However, observation is inconclusive and the wave field is dominated by the strong temporal periodicity.

For period-tripled breaking ($F = 4.57$ mm), three distinct phase orbits appear in figure 13(*c*) corresponding to the three breaking modes. Although modulation on a longer time scale may contribute to the noise in the inner orbits, noise in the outer

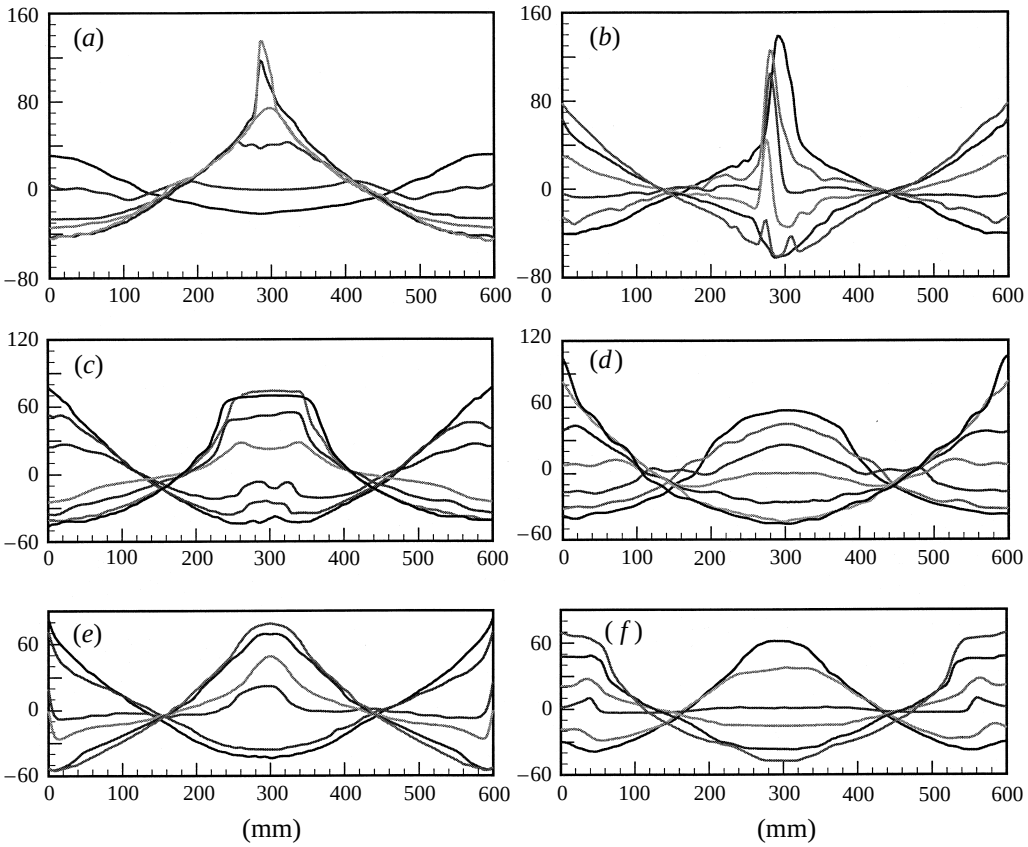

FIGURE 9. The detected wave profiles for modes A, B and C in figure 8. The vertical scale is 1.5 times the horizontal scale.

orbit for mode A is primarily the result of breaking events (note the phase-portrait paths are broader). Larger noise in the lower half of the orbit is due to jet penetration and rebounding during the trough phase ($\eta(0,t) < 0$). Oscillations in the upper-right corner of the diagram ($\eta \approx 80$ mm) reflect the variations in the sharp crest forms as shown in figure 8(*a*) and figure 12(*a*).

Compared to figure 13(*b*) for the non-breaking wave, the breaking-wave spectrum (figure 13*d*) has significantly-reduced amplitude for higher harmonics ($4f$, $5f$, $6f$, $\cdots$), while the background noise above $3f$ has increased significantly. The second harmonic for this breaking wave is as strong as that for the steep wave in figure 13(*b*). The modulation frequency appears as two spectral peaks $f/3$ apart to the side of $f = 1.60$ Hz. The upper modulation frequency components are larger than the lower two, indicating strong modulation of both the fundamental harmonic and the second harmonic. While the wave spectra show qualitative change between non-breaking waves and period-tripled breaking, the forcing spectra do not. A forcing spectrum for steep, but non-breaking waves is shown in figure 13 of Jiang *et al.* (1996). Even after period tripling, the forcing spectrum (not shown) consists of discrete harmonics with negligible background noise at all frequency including at the $f/3$ intervals. Therefore, the spectral peaks at $f/3$ intervals are due to the nonlinear interaction amongst the excited wave modes.

We extend the pseudo-phase diagram to three dimensions with coordinates ($\eta(t)$,

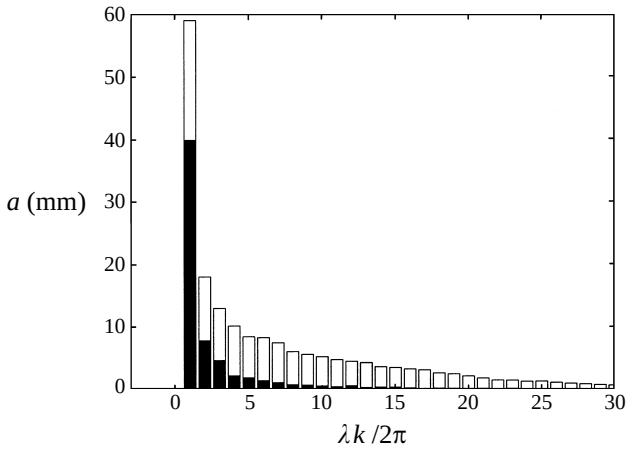

FIGURE 10. The maximum (hollow bar) and median (solid bar) wavenumber spectra for profiles in figure 9 where $\lambda = 600$ mm.

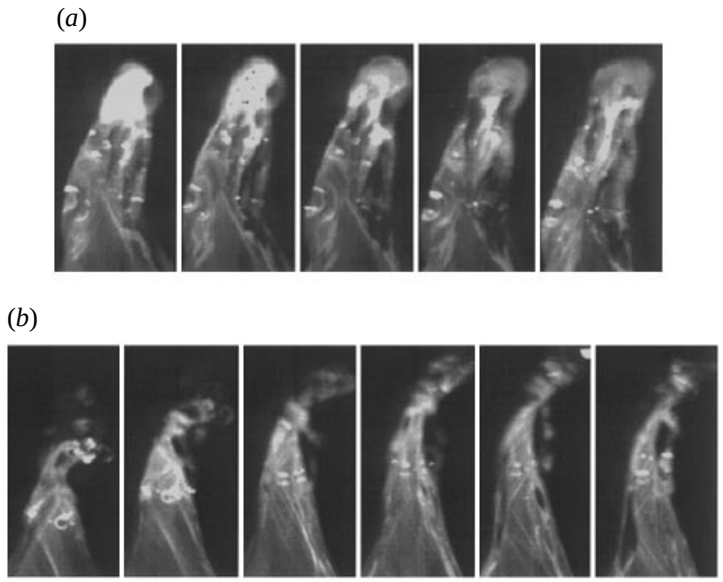

FIGURE 11. A magnified view of the crest in mode A at its maximum elevation. (*a*) $F = 4.57$ mm, $f = 1.60$ Hz. Time interval between each frame is 0.008 s. (*b*) $F = 4.60$ mm, $f = 1.61$ Hz. Time interval between frames is 0.016 s. Each frame is approximately 35 mm by 60 mm. Horizontal to vertical scale: 1:1.

$\eta(t+\tau)$, $\eta(t+2\tau)$) in figure 14. The essential feature is the same as shown in the two-dimensional surface, figure 13(*c*): there exist three different orbits corresponding to modes A–C. The dynamics of period tripling might be described by a low-dimensional system with an embedded dimension less than three. In figure 14(*a*), the grey-scale level of the trajectories is changed after every wave period and each level represents a unique mode. Furthermore, the 3-d phase diagram reveals that the outer trajectory (light grey) always connects to the intermediate orbit (black) and then to the orbit with the smallest area (dark grey) and goes back to the outer orbit (light grey) again. This represents the exact order of modes $A \rightarrow B \rightarrow C \rightarrow A \cdots$. Similar to figure 13(*c*),

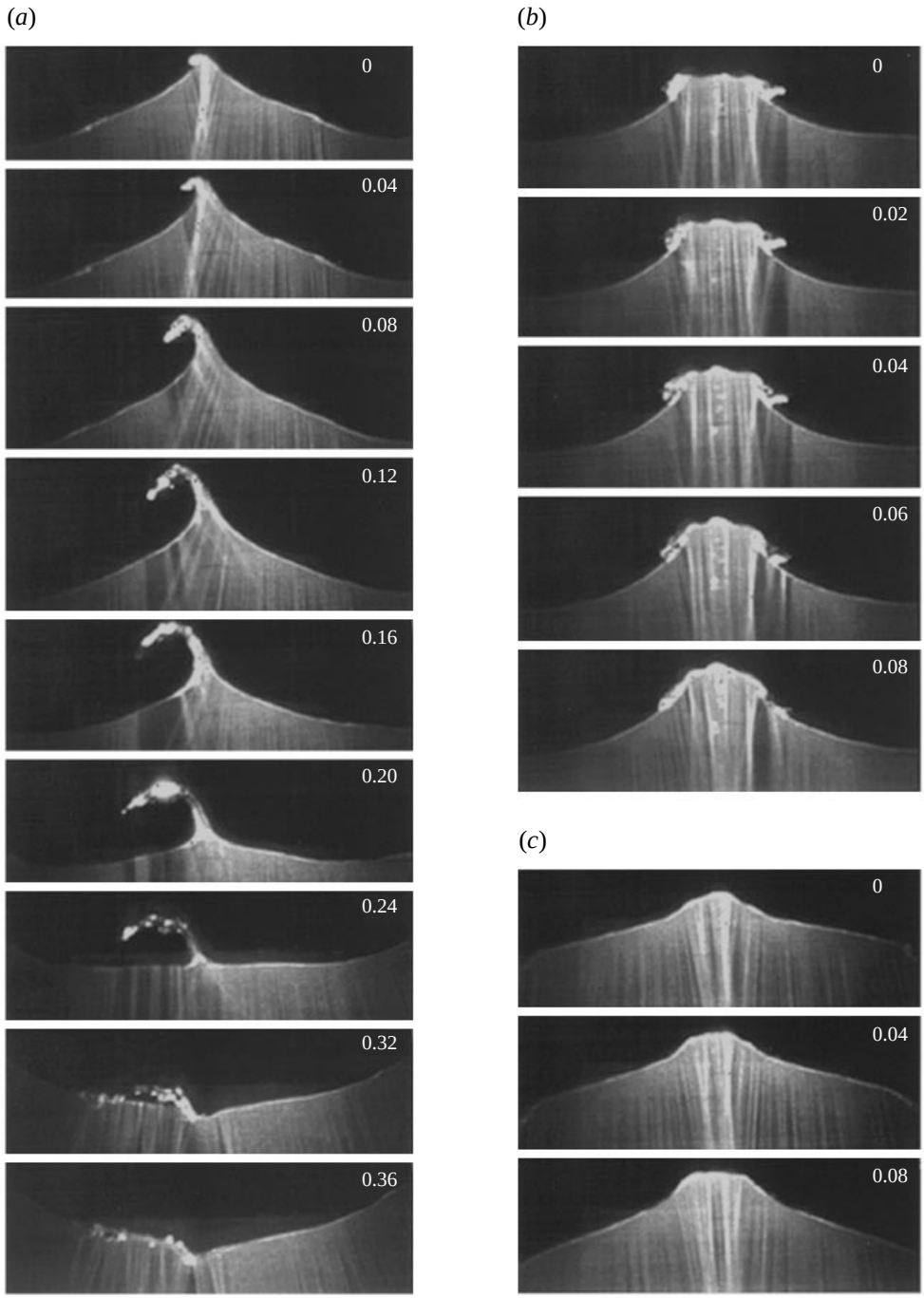

FIGURE 12. Three breaking modes with $F = 4.60$ mm and $f = 1.60$ Hz. Time (unit: s) is shown in each frame. (*a*) Mode A with 'leftward' plunging breaker, (*b*) double plunger to each side of the dimpled crest in mode B, (*c*) Mode C with maximum elevation at $t = 0.04$ s.

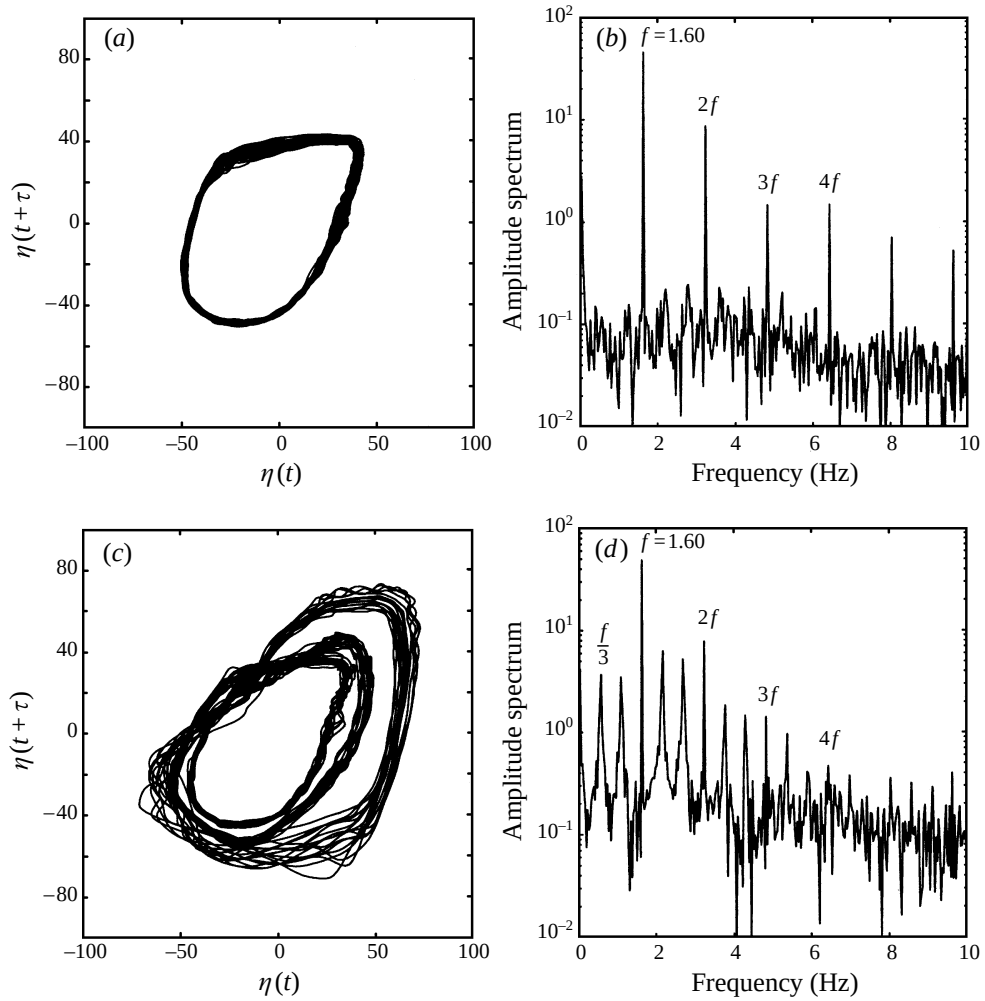

FIGURE 13. (*a*) Phase diagram and (*b*) amplitude spectrum for the elevation signal at the tank centre. Wave is steep, but not breaking ($f = 1.60$ Hz, $F = 4.15$ mm). The same for (*c*) and (*d*) except that period-tripled breaking occurs with $f = 1.60$ Hz, $F = 4.57$ mm. For (*a*) and (*c*) the time delay $\tau = 0.1$, s $= 0.16T$.

we find that choosing different time delay τ only alters the shape of the orbits, but not their width. Because of the strong dissipation through breaking, it is difficult to determine whether the orbit width is due to random noise or represents the extent of a torus in the phase space. A Poincaré map is constructed by taking a section $\eta(t) = 0$ through the three-dimensional pseudo-phase diagram. This is equivalent to choosing a wave period as the sampling delay in the time series that produces figure 14(*a*). The three clusters near the upper right (and the clusters near the bottom left) represent fixed points corresponding to the three modes. A similar Poincaré map of the non-breaking wave shows only one fixed point corresponding to a periodic state.

The spectrum reflects the global (averaged) characteristics; the possible interaction in the amplitude and phase of each harmonic is not shown in the Fourier analysis. The complete time series of wave elevation are shown in figure 15 and figure 16,

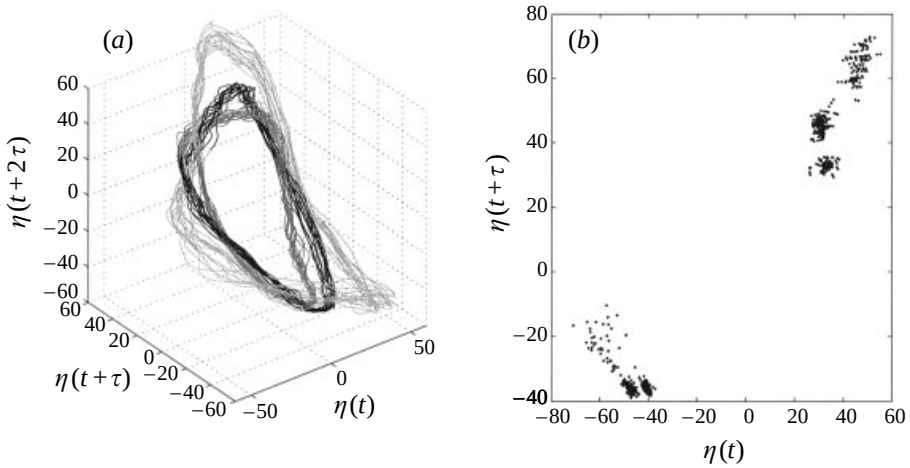

FIGURE 14. (*a*) Pseudo-phase space and (*b*) Poincare map corresponding to (*a*) for the same experiments shown in figures 13(*c*) and (*d*).

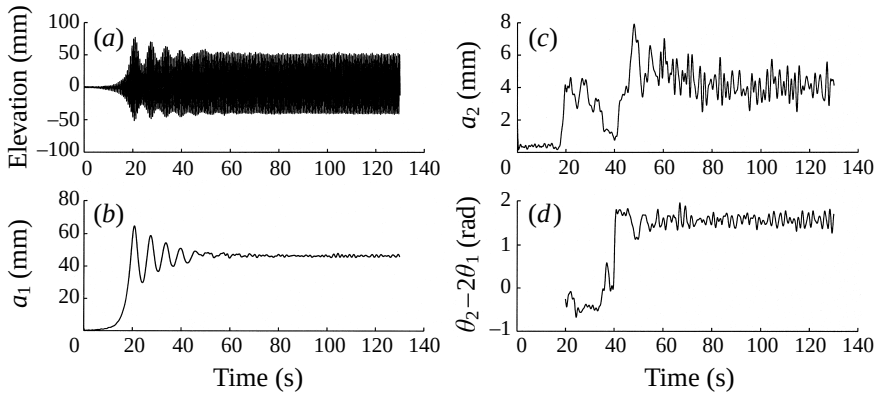

FIGURE 15. Complex-demodulated elevation for steep, non-breaking wave, $f = 1.60$ Hz and $F = 4.15$ mm. (*a*) The surface elevation as a function of time, (*b*) amplitude of the first harmonic, (*c*) amplitude of the second harmonic, and (*d*) phase-shift difference $\theta_2 - 2\theta_1$.

corresponding to the phase diagrams discussed above. Digital complex demodulation, a more versatile and informative technique in this case, is applied to demonstrate the interaction between the first two harmonics during period tripling and is discussed in the next section.

4.3. *Recurrent breaking and the second temporal harmonic*

The three steep waveforms discussed in § 3 – sharp crest in the numerics, flat and dimpled crest in our experiments, and round crest in the Penney & Price solution – closely resemble the waveforms that appear recurrently during period-tripled breaking. The essential nature of period tripling may then be linked with harmonic interaction that produces the diverse steep waveforms (§ 3). In particular, figure 13(*d*) shows a strong second temporal harmonic during period tripling. The recurrence of the three breaking modes and their likeness to the three steep waveforms suggest strong interaction between the first two harmonics and time-dependent $a_{1,2}$ and $\theta_{1,2}$. We apply complex demodulation (Bloomfield 1976) to determine $a_{1,2}(t)$ and $\theta_{1,2}(t)$ and to

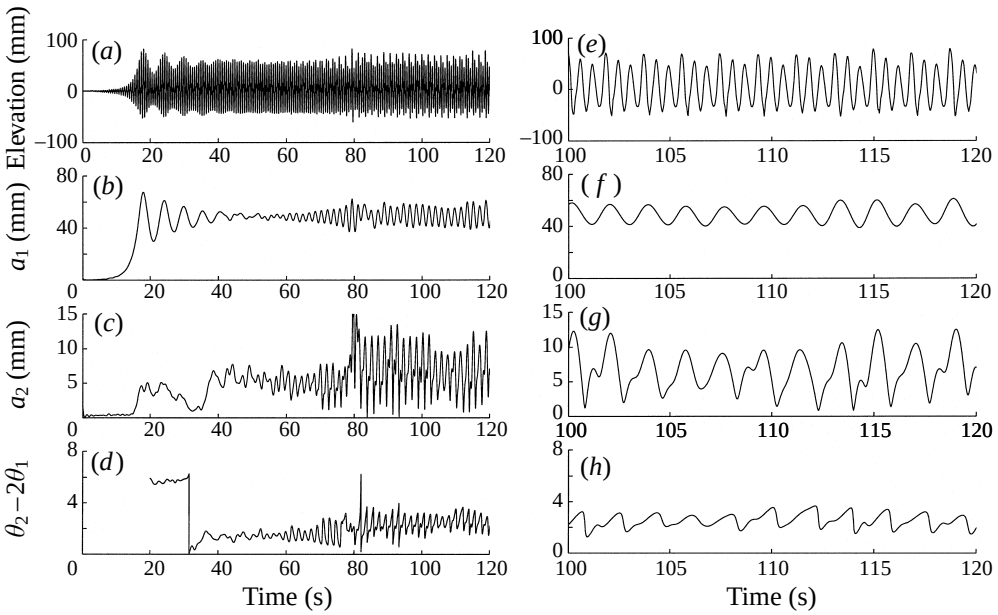

FIGURE 16. Complex-demodulated elevation for period-tripled breaking, $f = 1.60$ Hz and $F = 4.57$ mm. (*a*) Surface elevation; (*b*) a_1; (*c*) a_2; (*d*) phase-shift difference $\theta_2 - 2\theta_1$. (*e–h*), same graphs as (*a–d*) with magnified abscissa.

demonstrate the importance of the second harmonic during period-tripled breaking. Details of the procedure are given in the Appendix.

We first analyse a steep wave with a dimpled crest and no breaking. The elevation signal in figure 15(*a*) corresponds to the phase portrait and the Fourier spectrum in figure 13(*a*, *b*). The demodulated a_1 reaches a reasonably steady value at $t = 80$ s (figure 15*b*). As the wave approaches periodicity, a_2 grows to approximately 5 mm (figure 15*c*), about 10% of the first-harmonic amplitude a_1. Figure 15(*d*) shows that the phase-shift difference $\theta_2 - 2\theta_1$ jumps to about 0.5π, resulting in a dimpled crest form. Steep waves that we regard as temporally periodic in § 3 exhibit small but obvious oscillations of period $3T$ in $a_{1,2}$ after complex demodulation.

The periodic variation of $a_{1,2}$ becomes much larger in figure 16(*a–d*) when period-tripled breaking occurs. During wave growth, the two harmonics follow similar trends as in figure 15(*d*) for non-breaking waves. The oscillations in $a_{1,2}$ start around $t = 55$ s and grow slowly until the first breaker and the initiation of period tripling at $t \approx 82$ s, signalled by a jump in $\theta_2 - 2\theta_1$. Once period-tripled breaking occurs, the amplitude variations are about 10 mm for a_1 and about 5.5 mm for a_2. Figure 16(*d*) demonstrates that $\theta_2 - 2\theta_1$ oscillates between 0.3π and 1.1π, a much larger variation than that for non-breaking waves. The direct output of complex demodulation includes an additional phase shift that increases linearly with time. As its increase rate is exactly $f/3$, this phase shift is caused by the presence of strong neighbouring frequency components ($5f/3$ and $7f/3$) near the second harmonic with frequency $2f$. Therefore it is an artificial phase shift due to the limitation of the complex-demodulation procedure. The actual phase-shift difference between the first two harmonics is obtained by subtracting out this linearly increasing component and is presented in figure 16(*d*).

The magnified abscissas shown in figure 16(*e–h*) correspond to $t = 100$ s to $t = 120$ s in (*a–d*). The first-harmonic amplitude a_1 approximately reaches its max-

imum as does a_2 when the surface elevation is the largest (mode A), while a_2 is smaller and a_1 is at its smallest value when the maximum elevation is the smallest (mode C). During mode B, each amplitude is near its average value. Therefore the three distinct breaking modes correspond directly to the strong oscillation of the first two harmonics. The oscillation in η_0 is neglected and the combination of a_1 and a_2 explains approximately 80% of the elevation variation. Applying complex demodulation to higher harmonics shows that other harmonics are less significant: a_3 is only about 4% of a_1 with a_4 and a_5 even smaller.

4.4. *Comparison with other observations*

We have shown that the first two temporal harmonics are the most significant ones in the time series of period-tripled breaking. However, we do not yet understand the physical mechanism responsible for period tripling. Beside the mode interaction in parametric resonance, an even more complex factor may be the highly unsteady nature of breaking-wave dissipation. The time scale of the breaking-induced turbulence and its decay may be important in both triggering the sharp-crested breaking mode and maintaining the periodicity once period tripling occurs.

It is interesting to note that similar quasi-periodic breaking occurs for Faraday capillary waves. Goodridge, Shi & Lathop (1996) observed droplet ejection once every 12 (sometimes 14) forcing cycles, equivalent to six wave periods as compared to three periods in our experiments. Their observation may be interpreted as consecutive period doubling and period tripling. Our recent experiments in a circular cylinder with a 12 cm diameter also demonstrate period tripling for the subharmonic axisymmetric mode: the crest tends to be more bulbous at one cycle and becomes flatter in the following two cycles. The wave frequency is approximately 3.8 Hz. However, the period-tripled breaking is more robust and repeatable for Faraday waves in the rectangular cylinder.

Libchaber & Maurer (1980) observed competition between period-2 cycles and period-3 cycles in Rayleigh–Bénard experiments. The dissipative nature of the system seems to be critical for stable period tripling, as further shown in Arneodo *et al.* (1983) for a parametrically driven pendulum and for the Henon mapping. These studies are consistent with our observation that period tripling in Faraday waves is stable with wave breaking and that period tripling of Faraday waves in a circular cylinder is less robust and less repeatable without wave breaking (therefore less dissipation). Further analysis will require a better understanding of the dissipation process of wave breaking.

5. Energy and dissipation in breaking standing waves

We now give a brief account of the direct dissipation measurement, with an emphasis on the averaged breaking-wave dissipation. We first estimate work per wave period W with a non-overlapping time window. The window length is one wave period for non-breaking waves, or three wave periods for the triply-periodic breaking shown in figure 17. As stated in § 2.2, the growth in the wave amplitude (figure 17*a*) is accompanied by large oscillation in the measured power W (figure 17*b*). The difference $\mathscr{D} = W_3 - W_1$ is small compared to the mechanical loss W_1.

The time dependence of W during triply-periodic breaking is related to its unique dissipation mechanisms. To determine the slow oscillation in W, we integrate the force over a continuous, overlapping time window and apply a low-pass filter with a cut-off frequency of 3 Hz. The resulting W (figure 17*d*) has two peaks in every

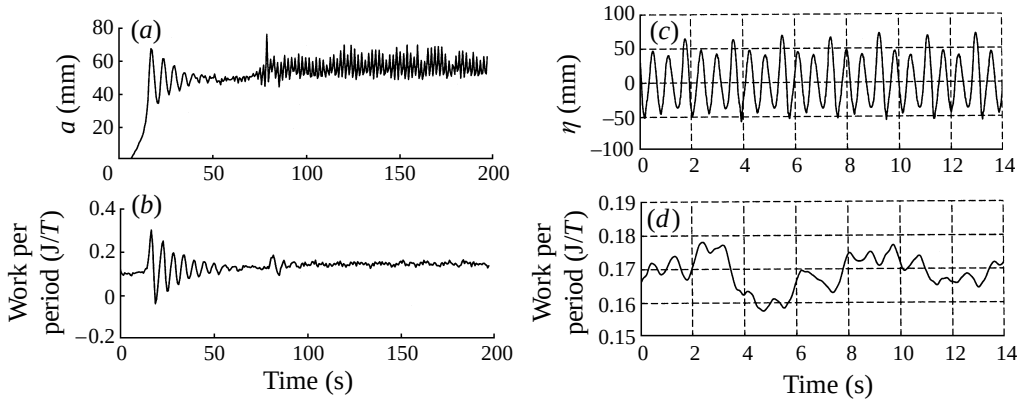

FIGURE 17. (*a*) Wave amplitude and (*b*) work per wave period (power, Joule/period) for period-tripled breaking, $f = 1.60$ Hz and $F = 4.57$ mm. (*c*) Surface elevation and (*d*) work per wave period during period-tripled breaking for $f = 1.61$ Hz, $F = 4.57$ mm.

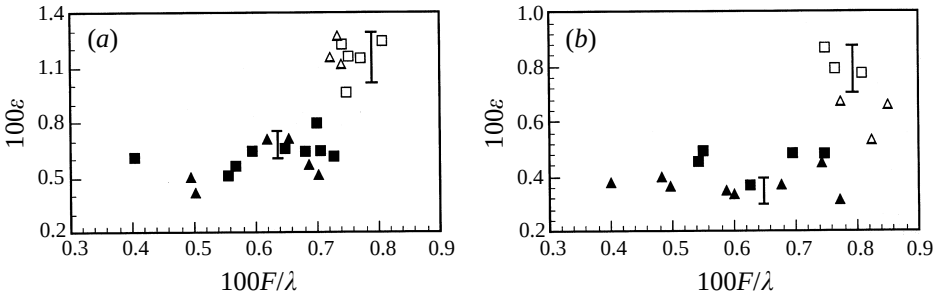

FIGURE 18. Dimensionless dissipation rate for non-breaking (▲ ■) and breaking waves (△ □) as a function of forcing amplitude. The error bars represent standard deviations due to non-overlapping windows for non-breaking and breaking waves. (*a*) $f = 1.59$ Hz (▲ △), $f = 1.60$ Hz (■ □), (*b*) $f = 1.61$ Hz (■ □), and $f = 1.62$ Hz (▲ △).

three-wave cycle (1.88 s). For example, between $t = 2$ s and $t = 4$ s, the first W maximum occurs slightly less than one period after the maximum elevation (mode A). The second peak occurs one and a half periods later. The most energetic breaking is the impinging jet as shown in § 4.1 and the ensuing air entrainment that lags the maximum wave elevation by one half-period. To compensate for this peak energy loss, there should be increased energy input, corresponding to the first peak in W. Since the same dissipation process occurs exactly one and a half periods later (at the two ends of the tank), the second peak in W is also expected.

The wave dissipation $\mathscr{D}$ is estimated by the procedure given in § 2.2. For example, $\mathscr{D}$ in figure 17(*a*, *b*) is calculated by subtracting the average W in stage 1 ($t = 0$–10 s) from the average W in stage 3 ($t = 100$–200 s). Our experiments have three control parameters: wavelength λ (limited by the tank configuration), forcing frequency ω_f and forcing amplitude F. Wave amplitude a and frequency ω_1 are both dependent parameters. Therefore, the dimensionless dissipation rate ε can be expressed as

$$\varepsilon = \frac{4\pi^2 \mathscr{D}}{\rho g b \lambda^3} = \varepsilon\left(\frac{F}{\lambda}, \frac{\omega_f}{2\omega_1}\right) \tag{5.1}$$

where b is the tank width. Dimensionless ε values are presented in figure 18 for four

f(Hz)	F_b (mm)	ε_1	ε_2	ε_{break}	SD
1.59	4.40	0.0060	0.0115	0.0055	0.0010
1.60	4.51	0.0065	0.0112	0.0047	0.0012
1.61	4.55	0.0043	0.0079	0.0036	0.0006
1.62	4.71	0.0036	0.0060	0.0024	0.0008

TABLE 2. Wave frequency f, threshold forcing amplitude F_b, and the corresponding dissipation rates. ε_1, dissipation rate for non-breaking waves; ε_2, dissipation rate for triply-periodic breaking; $\varepsilon_{break} = \varepsilon_2 - \varepsilon_1$, dissipation rate due to breaking. SD: the standard deviation for ε_{break}.

different forcing frequencies: 3.18, 3.20, 3.22 and 3.24 Hz. The dissipation data are slightly more scattered in figure 18(b) for $f = 1.61$ and 1.62 Hz than in figure 18(a) for $f = 1.60$ and 1.59 Hz. In the absence of breaking, ε slowly increases with forcing amplitude, although some data decrease at forcing amplitudes just below F_b, the threshold forcing for breaking. A boundary-layer estimate predicts a quadratic growth of dissipation rate ε for increasing wave amplitude. For period-tripled breaking, ε jumps to about twice the value for non-breaking waves, but does *not* increase for larger forcing amplitude. Therefore about 5% of the energy is dissipated over one wave period for steep, but non-breaking waves (based on the energy of a linear standing wave, $E = \frac{1}{4}\rho g b \lambda a^2$), while breaking increases the dissipation per temporal period to about 10% of the total wave energy.

The error bars in figure 18 represent the data scatter caused by the use of non-overlapping time windows in the dissipation estimate. Their large values reflect partially the modulation in the steep waves and the strong interaction during triply-periodic breaking (figure 17c). Since we are interested in the average dissipation, we use overlapping time windows of 50 wave periods for integration and denote the average dissipation per wave period as $\overline{\mathscr{D}}$. The standard deviation is drastically reduced to 0.5% for non-breaking waves and is reduced to 2% for breaking waves by replacing $\mathscr{D}$ in equation (5.1) with $\overline{\mathscr{D}}$.

Breaking-wave dissipation ε_{break} is defined as the increase in wave dissipation from a non-breaking wave (ε_1) to triply-periodic breaking (ε_2), our best and only estimate for the breaking case. For each forcing frequency in figure 18, the dissipation rate ε has considerable scatter for both triply-periodic breaking and non-breaking waves. Thus, we calculate ε_1 by averaging the dissipation rates for the largest four forcing amplitudes with $F < F_b$, where F_b is again the threshold forcing amplitude for breaking. As a result, ε_1 represents viscous and contact-line dissipation close to the limiting wave steepness. Similarly, we estimate ε_2, the dissipation due to breaking plus viscous and contact-line dissipation, by averaging the dissipation rates for $F > F_b$ (hollow symbols in figure 18).

Table 2 lists F_b, ε_1, ε_2, and ε_{break} for the four wave frequencies. The largest breaking-wave dissipation $\varepsilon_{break} = 0.0055 \pm 0.0010$ occurs for $f = 1.59$ Hz, consistent with its largest total wave dissipation ε_2. Increasing forcing frequency reduces the breaking-wave dissipation. We believe this frequency dependence is related to the effect of forcing frequency on the jet formation (spray) and the collision intensity (splash). With lower forcing frequency, the sharp crest has more time to develop, thus the subsequent impinging process generates more air entrainment and more turbulence.

6. Concluding remarks

We further verify that the steep standing wave forms observed by Jiang *et al.* (1996) are the result of interaction between the first and second temporal harmonics. Increasing the forcing amplitude leads to a wave steepness very close to the limiting steepness for gravity standing waves. Gentle breakers form at the crest as shown in Jiang *et al.* (1996) but are unstable at even larger forcing amplitude. Period tripling follows with three breaking modes – mode A: sharp crest forms, the upward jet or a large plunger to either side impinges on the wave surface; mode B: flat or dimpled crest forms, with outward plungers to each side of the crest; mode C: the crest is round and smooth with no significant breaking. The most conspicuous feature of period tripling is its robustness. With large forcing amplitude, it appears at every wave frequency close to the linear natural frequency.

The most energetic breaking of standing waves is exemplified by the jet break-up in mode A and the subsequent air entrainment. Secondary breaking occurs in mode B with spilling and small plungers to each side of the flat crest. The sharp crest in mode A has an angle less than 30°, and it remains two-dimensional until the upward jet disintegrates. These steep waveforms and breaking modes can cause drastically different radar returns due to wedge-scattering mechanisms.

The phase portraits for both non-breaking waves and period-tripled breaking are reconstructed from the wave elevation signal at $x = 0$. A periodic steep wave corresponds to a single orbit in the phase diagram, but modulation noise signals quasi-periodic behaviour. The phase diagram for period-tripled breaking is qualitatively different – three orbits appear corresponding to each breaking mode. Period tripling manifests itself in the amplitude spectrum as discrete spectral peaks $f/3$ apart, where f is the subharmonic wave frequency. The wave spectrum for period-tripled breaking also shows larger background noise than that for non-breaking waves. The first two temporal harmonics (f and $2f$) remain strong during period tripling, but the amplitudes of harmonics above $3f$ are significantly reduced. Complex demodulation of the elevation signal reveals strong variations in the first two temporal harmonics during period-tripled breaking. Furthermore, the interaction between these two modes corresponds directly to the three breaking modes.

We provide direct measurements of the energy dissipation due to viscous and contact-line effects, and due to breaking. The instantaneous support force is integrated with respect to tank displacement to provide the system energy input. Wave dissipation is then obtained through energy balance for a periodic wave field. Breaking waves approximately double the total wave dissipation over non-breaking waves. Temporal variations during triply-periodic breaking are attributed to the strength of the different breakers: mode A provides the largest dissipation because of the re-entrant jet and air entrainment. Strong frequency dependence is shown in both the total dissipation rate ε and the dissipation rate due to breaking ε_{break}. The maximal ε_{break} is 0.0055 ± 0.0010 for $f = 1.59$ Hz.

The outstanding questions concern the precise mechanism that triggers and maintains the period tripling, even under violent breaking-wave conditions, and the condition, at least qualitatively, for nonlinear interaction between admissible harmonics. The phase diagram and complex-demodulation analyses suggest that these two questions are closely related. In addition, the wave spectrum suggests period tripling even prior to breaking and a strong second harmonic for both non-breaking waves and period-tripled breaking. Modelling internal resonance by lower-mode truncation has been explored by many for three-dimensional waves (Feng & Sethna 1989; Nagata

1989; Miles & Henderson 1990), while similar models for two-dimensional waves remain to be solved. We are currently examining analytical and numerical models to qualitatively describe period tripling.

Finally, we mention a similarity between our results with those of Srokosz (1981). A fully nonlinear boundary-integral method is used in Srokosz's work to simulate gravity standing waves and the effect of wave reflection on breaking. In two particular cases, Srokosz used linear standing waves with unrealistically large amplitude as initial conditions. Although his computations failed after about one half wave period, they show either a very high wave with a sharp crest at the centre, or a flat crest with two plungers extending to each side. The similarity between his results and breaking modes A and B again demonstrates the unique nonlinear dynamics shared by both free standing waves and Faraday waves. The true nature of the strong nonlinearity in standing waves can thus be captured by careful Faraday wave experiments.

This research was supported by the Office of Naval Research partially under contract number N00014-93-1-0867 and partially under the University Research Initiative – Ocean Surface Processes and Remote Sensing at the University of Michigan, contract number N00014-92-J-1650. The suggestions of two referees are gratefully appreciated.

Appendix. Digital complex demodulation

Complex demodulation, as described by Bloomfield (1976), may be regarded as a local harmonic analysis that offers both the amplitude and the phase of a certain frequency component in a time series. In the case of signals with multiple frequency peaks, the task of distinguishing between the frequency components of interest and other components or noise can be achieved by a bandpass filter centred about the frequency of interest. However, to be consistent with Bloomfield (1976), we first shift the frequency by an amount $-\omega$, then apply a low-pass filter to obtain the modulated amplitude and phase of the carrier wave with frequency ω. The pass band is chosen to remove all the sum frequencies, higher harmonics, and noise, but to admit the bandwidth of the carrier wave due to amplitude and phase modulation. Procedures and algorithms are available in Bloomfield (1976). Note that our elevation signal has discrete harmonics, i.e. the signal is narrow-banded. More sophisticated multi-resolution techniques such as wavelet analyses are not necessary for our purpose as we are not interested in the high-frequency components of the signal.

This flexible technique is most suited for the simultaneous measurement of the amplitude and phase of a narrow-banded modulated carrier signal as a function of time. However, it has several underlying assumptions. (1) The carrier signal must be narrow-banded around the target frequency for which there is a close but not necessarily accurate estimate. (2) The original amplitude and phase modulation before sampling must be smooth and continuous. (3) The modulation frequency is much smaller than the carrier frequency. The first two assumptions are satisfied for the case of a forced Faraday wave. Knowing that the wave frequency is one half of the forcing frequency, we want to establish the connection between period tripling and the modulation of the first and the second temporal harmonics. Even for triply-periodic breaking, the modulation for the low-frequency harmonics can still be assumed to be smooth as the breaking event is local and affects only the higher frequency harmonics as shown in § 4.2.

The third assumption is related essentially to the filter design. A low-order filter will suffice when the modulation signal is extremely narrow-banded. Since the time scale of the modulation is only three times that of the carrier signal in the period

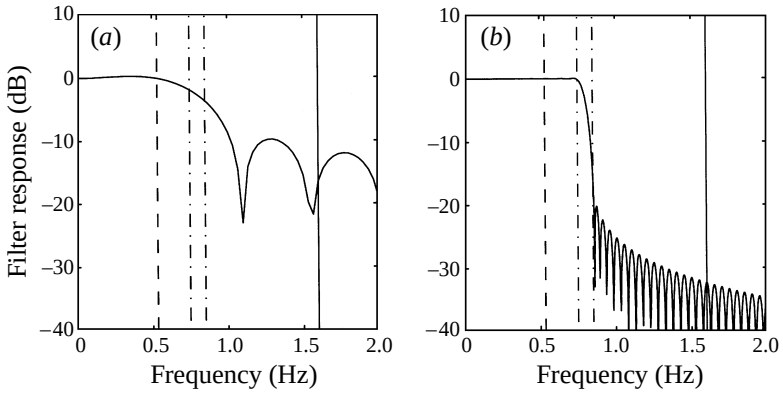

FIGURE 19. Effect of sampling rate on the FIR filter design with (*a*) $f_s = 300$ Hz; (*b*) $f_s = 30$ Hz. ——, carrier frequency $f = 1.60$ Hz; – – –, target modulation frequency; — · —, transition band.

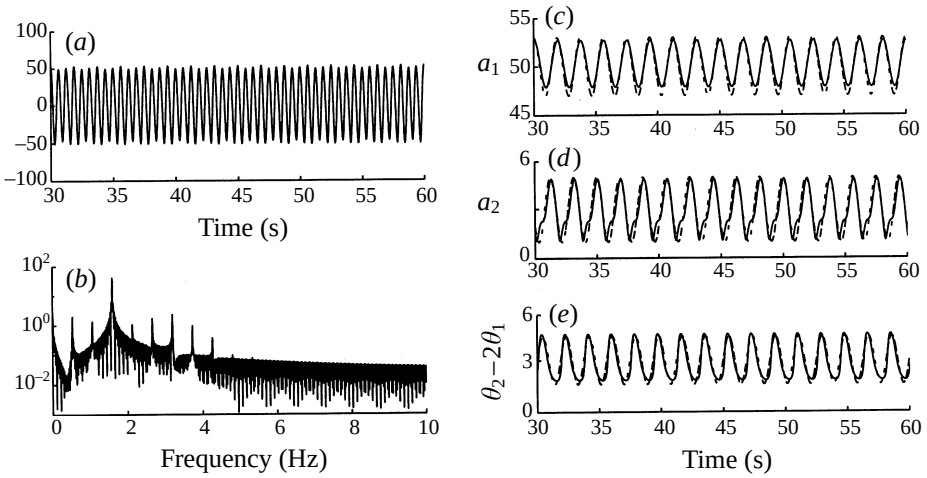

FIGURE 20. Effectiveness of complex demodulation for triply-periodic signal, carrier wave frequency $f = 1.6$ Hz. (*a*) $y(t) = a_1 \cos(2\pi f t + \theta_1) + a_2 \cos(4\pi f t + \theta_2)$; (*b*) spectrum of a discretized signal $y(t)$; (*c*) $a_1 = 50 + 3\cos(2\pi f t/3)$; (*d*) $a_2 = 3 - 2\sin(2\pi f t/3)$; (*e*) $\theta_2 - 2\theta_1 = \pi + \sin(2\pi f t/3)$. - - - - -, Actual amplitudes and phase shift; ——, estimated values from a complex demodulation of the discrete signal ($f_s = 30$ Hz).

tripling, special care must be taken in the filter design: it must admit the inherent $\frac{1}{3}f$ sidebands around the carrier signal with frequency f, while blocking the $\frac{2}{3}f$ sidebands due to the modulation of adjacent harmonics. For the time series herein, we use digital linear-phase FIR filters designed by the least-squares minimization method (figure 19). The linear phase response is critical to accurate phase angle measurement. The least-squares minimization approach gives a flatter response in the pass band than most windowing approaches, while maintaining a good blocking response in the stop band. More information about this type of filter can be found in standard Digital Signal Processing (DSP) texts (e.g. Proakis & Manolakis 1996).

The digital filter chosen for complex demodulation (figure 19) has three bands: a pass band with a cut-off frequency at $[0, \frac{1}{2}f - \delta]$, a transition band at $[\frac{1}{2}f - \delta, \frac{1}{2}f + \delta]$, and a stop band for $[\frac{1}{2}f + \delta, \frac{1}{2}f_s]$. Here, 2δ is the transitional bandwidth and $\frac{1}{2}f_s$ is the Nyquist frequency (f_s: sampling frequency). The period-tripled modulation sets an

upper limit for the transitional bandwidth as we must exclude the modulation signal caused by other harmonics. $\delta = \frac{1}{32}f$ is found to give a good transitional response. However, as the order of such FIR filters (number of coefficients) increases for a narrower transition band, 6000 coefficients are required for a time series sampled at 300 Hz. Such an operation is expensive and impractical (with Matlab software on an HP9000 workstation).

This problem is alleviated by reducing the sampling frequency, thus reducing the filter order proportionally (figure 19). Since we are interested in the modulation frequency around $\frac{1}{3}f \approx 0.53$ Hz, a reduced $f_s = 30$ Hz is sufficient. Such an operation is called decimation in DSP (Proakis & Manolakis 1996). In figure 19, two filters with different sampling frequencies are shown using the above specifications ($f = 1.60$ Hz). Using the same number of coefficients (600), a filter with $f_s = 30$ Hz has a much flatter response in the pass band, a much quicker response decay in the transition band and a better stop-band response. The transition band reduces the signal amplitude by -20 dB.

Hence, we first transform the time series (sampled at 300 Hz) to $f_s = 30$ Hz, and shift the whole record by $-f$ in the frequency domain (f is the carrier wave frequency). We then apply the FIR filter twice to the shifted time series in both the forward and backward direction. This eliminates any phase lag introduced by the filtering and doubles the filter order. To obtain the amplitude and phase of the second harmonic, we only need to change the shifting frequency from $-f$ to $-2f$. A sample signal with period-tripled modulation is shown in figure 20. The demodulated amplitudes for the first and second harmonics exhibit slight differences with the actual amplitudes, but the phase difference agrees more closely. Complex demodulation provides the temporal evolution of a frequency harmonic, unavailable from other time-series analysis.

REFERENCES

Arneodo, A., Coullet, P., Tresser, C., Libchaber, A., Maurer, J. & d'Humieres, D. 1983 On the observation of an uncompleted cascasde in a Rayleigh-Benard experiment. *Physica* D **6**, 384–392. (Also in *Chaos* (ed. B. L. Hao). World Scientific.)

Benjamin, T. B. & Ursell, F. 1954 The stability of the plane free surface of a liquid in vertical periodic motion. *Proc. R. Soc. Lond.* A **225**, 505–515.

Bloomfield, P. 1976 *Fourier Analysis of Time Series: An Introduction*, pp. 118–149. Wiley.

Bryant, P. J. & Stiassnie, M. 1994 Different forms for nonlinear standing waves in deep water. *J. Fluid Mech.* **272**, 135–156.

Decent, S. P. & Craik, A. D. D. 1955 Hysteresis in Faraday resonance. *J. Fluid Mech.* **293**, 237–268.

Feng, Z. C. & Sethna, P. R. 1989 Symmetry-breaking bifurcation in resonant surface waves. *J. Fluid Mech.* **199**, 495–518.

Goodridge, C. L., Shi, W. T. & Lathrop, D. P. 1996 Threshold dynamics of singular gravity-capillary waves. *Phys. Rev. Let.* **76**, 1824–1827.

Jiang, L., Ting, C., Perlin, M. & Schultz, W. W. 1996 Moderate and steep Faraday waves: instabilities, modulation and temporal asymmetries. *J. Fluid Mech.* **329**, 275–307.

Libchaber, A. & Maurer, J. 1980 Une experience de Rayleigh–Bénard de geometrie reduite: multiplication, accrochage, et demultiplication de frequences. *J. Phys. Paris* C3 **41**, 51–56.

Longuet-Higgins, M. S. 1963 The generation of capillary waves by steep gravity waves. *J. Fluid Mech.* **16**, 138–159.

Longuet-Higgins, M. S. 1980 On the forming of sharp corners at a free surface. *Proc. R. Soc. Lond.* A **371**, 453–478.

Mercer, G. N. & Roberts, A. J. 1992 Standing waves in deep water: their stability and extreme form. *Phys. Fluids* A **4**, 259–269.

Miles, J. W. & Henderson, D. M. 1990 Parametrically forced surface waves. *Ann. Rev. Fluid Mech.* **22**, 143–165.

Moon, F. C. 1992 *Chaotic and Fractal Dynamics: An Introduction for Applied Scientists and Engineers* Wiley.

Mullin, T. 1993 *The Nature of Chaos*. Oxford University Press.

Nagata, M. 1989 Nonlinear Faraday resonance in a box with a square base. *J. Fluid Mech.* **209**, 265–284.

Packard, N. H., Crutchfield, J. P., Farmer, J. D. & Shaw, R. S. 1981 Geometry from a time series. *Phys. Rev. Lett.* **45**, 712–716.

Penney, W. G. & Price, A. T. 1952 Finite periodic stationary gravity waves in a perfect liquid. *Phil. Trans. R. Soc. Lond.* A **244**, 254–284.

Perlin, M., Bernal, L. P. & He, J. 1996 An experimental study of deep water plunging breakers *Phys. Fluids* **8**, 2365–2374.

Perlin, M., Lin, H. & Ting, C. 1993 On parasitic capillary waves generated by steep gravity waves: an experimental investigation with spatial and temporal measurements. *J. Fluid Mech.* **255**, 597-620.

Proakis, J. G. & Manolakis, D. G. 1996 *Digital Signal Processing: Principles, Algorithms, and Applications*. Prentice Hall.

Schultz, W. W. & Vanden-Broeck J. M. 1990 Computations of nonlinear standing waves. *Bull. Am. Phys. Soc.* **35**, 2290.

Schultz, W. W., Vanden-Broeck, J. M., Jiang, L. & Perlin, M. 1998 Highly nonlinear standing water waves with small capillary effect. *J. Fluid Mech.* **369**, 253–272.

Schwartz, L. W. & Whitney, A. K. 1981 A semi-analytic solution for nonlinear standing waves in deep water. *J. Fluid Mech.* **107**, 147–171.

Srokosz, M. A. 1981 Breaking effects in standing and reflected waves. *Hydrodynamics in Ocean Engineering*, pp. 183–202. Norwegian Inst. Tech.

Tadjbakhsh, I. & Keller, J. B. 1960 Standing surface waves of finite amplitude. *J. Fluid Mech.* **8**, 442–451.

Takens, F. 1980 Detecting strange attractors in turbulence. *Dynamical Systems and Turbulence* (ed. D. A. Rand & L. S. Young), pp. 366–381. Springer.

Taylor, G. I. 1953 An experimental study of standing waves. *Proc. R. Soc. Lond.* A **218**, 44–59.

Ting, C. L. & Perlin, M. 1995 Boundary conditions in the vicinity of the contact line at a vertically oscillating upright plate: an experimental investigation. *J. Fluid Mech.* **295**, 263–300.

Vanden-Broeck, J. M. & Schwartz, L. W. 1981 Numerical calculation of standing waves in water of arbitrary uniform depth. *Phys. Fluids* **24**, 812–815.